Proceedings of ASME Turbo Expo 2014: Turbine Technical Conference and Exposition
GT2014
June 16 - 20, 2014, Düsseldorf, Germany

AN OPTIMIZATION OF AN INDOOR ENGINE TEST FACILITY FOR PROPELLER TESTS WITH HIGH FLOW RATES

H. H.-W. Funke **J. Keinz**
Aachen University of Applied Sciences
Aachen, Germany

T. Pohlmann **R. Heinze** **F. Kameier**
Düsseldorf University of Applied Sciences
Düsseldorf, Germany

K. Schlich
RED Aircraft GmbH
Adenau, Germany

ABSTRACT

A new aviation propulsion system configuration with a propeller configuration at high flow rates driven by a newly developed 12-cylinder 370 kW kerosene piston engine was investigated in an indoor engine test facility. The outlet duct performance of the test facility choked the propeller for flow rates at design conditions and caused low frequency flow rate fluctuations A steady-state operation of propeller was not possible.

To visualize the flow field in the facility and to evaluate several improvements, a simplified CFD calculation with a new approach for the propeller flow field was performed. The method was verified with flow field measurements around the propeller in the facility.

It was necessary to carry out the numerical calculations for the whole test facility with inlet and outlet duct systems. This was the only way all parts of the pressure loss could be taken into account. The special adapted model of the propeller flow with a sink and a source of mass flow and with a radial distribution of the outlet swirl is not known from the literature and has not been published before. In particular, the radial distribution of the swirl was designed according to the velocity profile of a Hamel-Oseen-Vortex with a typical maximum at 75% rotor span. The sink/source approach permits a high accuracy of the flow topology and the pressure loss calculations through a comparatively high mesh resolution in the duct system and the test cell - no propeller mesh is necessary.

Large unstable recirculation zones in the test chamber were detected which in turn lead to a newly designed collector cone. Hence, low frequency flow rate fluctuations of the propulsion system were eliminated and the necessary mass flow through the test facility was provided.

INTRODUCTION

Based on restrictions of noise and weather conditions, investigations of propeller characteristics are only possible using indoor test beds. Therefore, indoor engine and propeller test facilities provide a closed and sound-damped weather-independent testing environment.

The indoor engine–propeller test facility of Aachen University of Applied Sciences (AcUAS) supports Raikhlin Aircraft Engine Development' (RED) newly developed RED A03 12-cylinder 370 kW kerosene piston engine development and certification process. The certification specifications for piston engines according to CS-E require intensive testing of the engine with propeller operation.

During first trial runs of the engine-propeller system, propeller vibrations and a periodic oscillation of the rotational speed were observed. Furthermore oil pressure fluctuations of the propeller governor were observed while trying to establish constant rotational speed by adjusting the propeller blades.

To analyze the phenomena responsible for these observations experimental measurements of the flow topology inside the engine-propeller test cell were performed. A large recirculation of air affecting the complete test cell aerodynamics and a blockage of the air outlet duct collector system was discovered.

This paper presents the experimental work and a new sink/source approach for the numerical procedure resulting in modifications of the indoor-engine-propeller test facility.

PROPULSION SYSTEM TEST FACILITY OF AACHEN UNIVERSITY OF APPLIED SCIENCES

The indoor aircraft engine test facility of the University of Applied Sciences in Aachen, Germany, was built in the 1960ies and offers several test stands for education and research on IC engines for automotive applications, small stationary turbo shaft gas turbines, jet engines and propellers.

This jet engine and propeller test facility (Figure 1) is located below ground and is about 42 m in length with a width of about 14 m and a total volume of 2000 m³. It supports two test beds arranged in parallel so the whole room has an asymmetric character.

One test bed is used for jet engines up to 50 kN static thrust also being capable of installing afterburners with an exhaust gas temperature up to 1800 K. The other test bed can support propeller engines up to 400 kW power and a propeller diameter of 2.2 m as shown in Figure 1. Due to the use of the test cell for different purposes the general layout of the indoor-engine-propeller test cell with its asymmetric position of the test beds is not built according to the SAE recommendations for turboprop test cells [1]. The inner test cell dimensions are 14 m in length, 8.1m width and 4.8 m height (see Figure 1 C).

Multiple measurement applications allow vibration and strength analyses, investigations of the aerodynamic and thermal behavior of the engines as well as exhaust gas analyses. The total maximum air mass flow of the test cell is 350 kg/s designed for differential pressures up to 500 mm WC. The air supply is provided by an air inlet duct system delivering fresh air into the test stand from the outside ground level 11 m above. Air from the propeller test bed and exhaust gases from the jet engines are discharged back up to the ground level and into the atmosphere by outlet duct systems and chimneys located in the installation axis of each engine.

For noise emission reduction the test stand ceiling and walls are equipped with 150 mm thick sound absorbing material protected against abrasion, negative pressure and mechanical loads by a corrosion resisting perforated sheet metal surface. The air inlet system sound absorber consists of three rows with 60 sound absorbing cascades in total allowing air speeds up to 40 m/s. The outlet duct system is designed as a combined interference-absorption sound protection system with a successive enlargement of cross section and several resonance chambers of different sizes ensuring a free discharge of air from the propeller test bed and hot exhaust gases from the jet engine test bed as well. Details on the test facility can be found in [2].

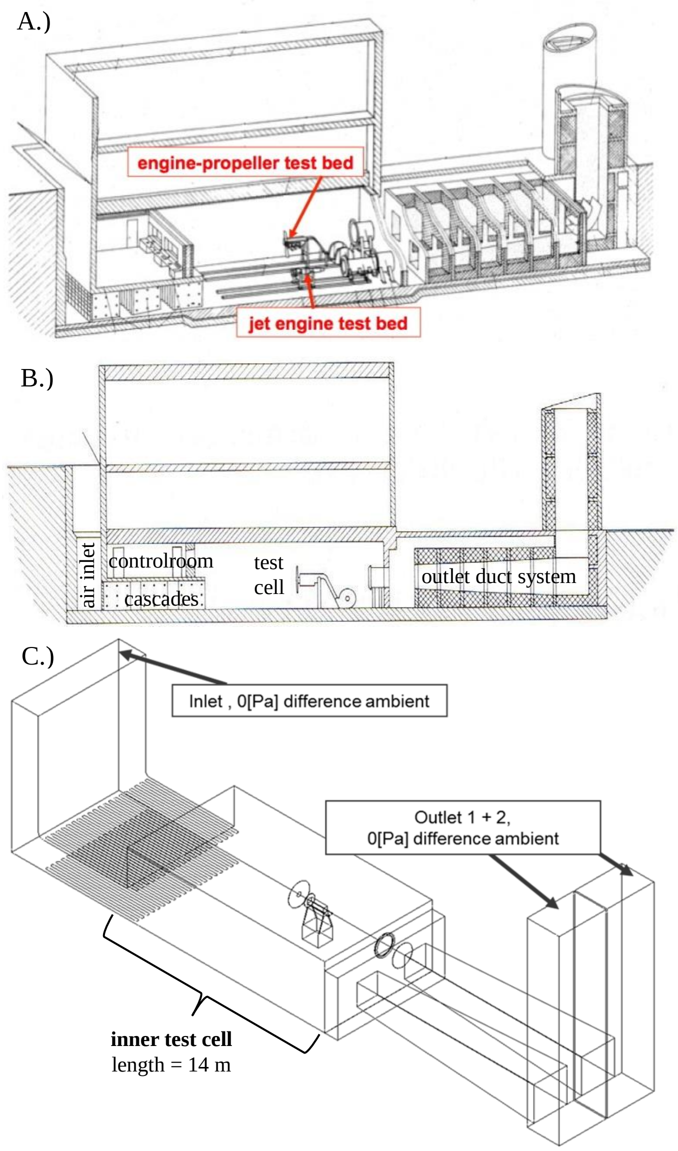

Figure 1: Aero Engine Test Facility at AcUAS:
A.) isometric view of the test cell,
B.) cross-section of the test cell,
C.) computational domain of the test cell used for CFD.

Table 1: Performance Data of RED A03

Rating	Engine speed [rpm]	Propeller speed [rpm]	Propeller Torque [Nm]	Shaft Power [KW]/[HP]	BSFC [g/KWh]
Take-off, SL	4000	2127	1650	368/500	235
Max. continuous, FL65	3750	1995	1688	353/460	230
Best economy, SL	3500	1862	1510	294/400	222

INSTALLED PROPULSION SYSTEM RED A03

The installed propulsion system is the newly developed piston engine RED A03 powering a 5-blade constant speed propeller. It is a 370 kW water-cooled, 12-cylinder, 6134 cm³ capacity heavy fuel engine in V-80° configuration with 4 overhead spur-geared camshafts (double overhead camshaft DOHC) and 4 valves per cylinder. An overview of the engine performance data is given in Table 1.

The propeller is driven by a flanged, single stage, reduction transmission, fitted in front of the engine (reduction ratio 1:1.88). The engine is approved for both pusher and tractor applications. The propeller MTV-5-1-E-C-F CFL210-56 is a hydraulically controlled 5-blade constant speed propeller with a diameter of 2.1 m, with counterweights, without feathering and without reverse. The blades are natural-composite with fiber reinforced epoxy cover, metal erosion shields and acryl varnish. The rotational direction of the propeller-engine system is anti-clockwise.

EXPERIMENTAL ANALYSIS OF TEST FACILITY

During the first trial runs of the engine RED A03 in propeller operation, vibrations of the propeller and fluctuations in the propeller rotational speed were observed. The on-speed governor of the propeller was not able to handle the severe flow disturbances occurring in the test cell, resulting in periodic fluctuations of the rotational speed of the propeller every 5 seconds (Figure 20, --- w before Mod). At a chosen rotational speed the time averaged point of operation of the engine was reduced as well. This results in a reduced fuel flow to the engine (Figure 20, -·- FF before Mod) compared to operation at a stable engine power. As a result of the instabilities the desired points of operation for the engine operation, e.g. full load Take-Off condition, could not be achieved.

At first based on a smoke visualization of the respective flow inside the test cell using a smoke-generator, the experimental measurement of the characteristic flow field inside the test facility was done by means of a portable Prandtl-Probe supported by a twine-probe. Since the periodic fluctuations have also been observed the flow measurements can only give a quasi-stationary averaged value of flow velocity and flow direction as an estimate of the respective flow phenomena.

Figure 2 shows the top view of the indoor propeller and jet engine test facility in the mid-plane of the propeller at a ground distance of 2.18 m. On the left side the engine-propeller test bed is illustrated schematically, on the right the jet engine test bed is also depicted exemplary. At defined measurement positions the measured direction and velocity magnitude of the air are plotted as vectors.

The measurements show that a significant portion of the propeller air flow is not exiting the test cell via the exhaust duct supported by the swirl of the air flow behind the propeller. This creates a large recirculation zone covering a significant area of the test cell. Parts of the air jet exiting the propeller recirculate back to the inlet of the propeller which is presumably responsible for the observed rotational speed fluctuations (w).

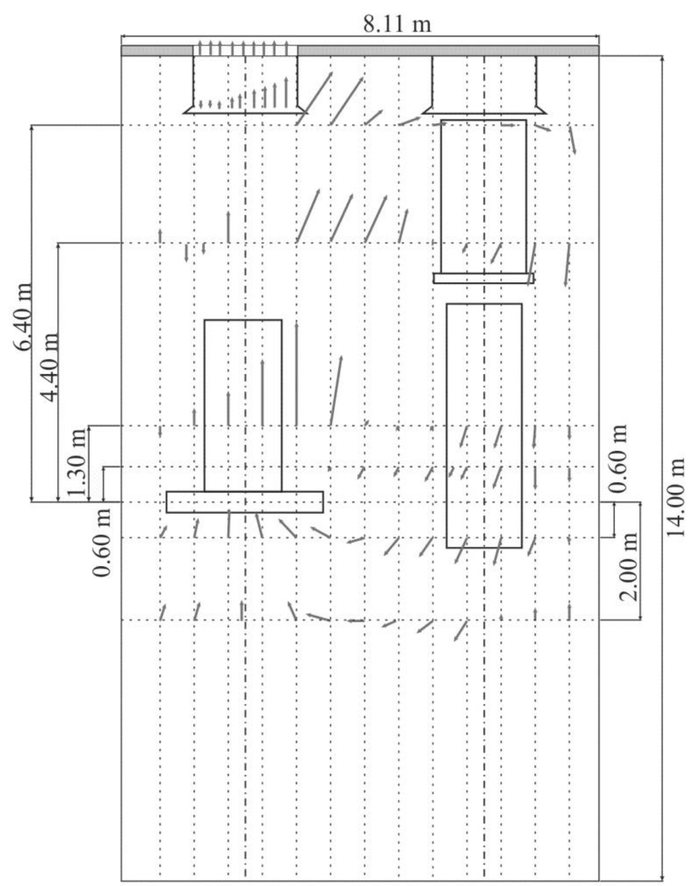

Figure 2: Measured Flow Field of inner test cell of the Test Facility (mid-plane view 2.18 m above the ground), anti-clockwise rotation.

Another important finding from the flow measurements can be seen at the propeller air outlet duct. A small recirculation flow of air at the left corner is blocking parts of the outlet cross section. This points to an insufficient size of the outlet area combined with an aerodynamic flow blockage of the outlet duct system. It is to assume that only a small portion of the air mass flow passing the propeller is exiting the test cell via the outlet duct system.

Based on these findings necessary modifications of the test cell outlet duct system should be defined, supported by numerical investigations of the flow field in the indoor test cell. At first the given configuration is to be investigated for comparison of the measured flow phenomena. Based on this comparison geometrical modifications can be investigated in the numerical simulation. An important parameter for optimization is the mass flow balance passing the propeller and entering/exiting the test cell. Based on the flow field inside the test cell for the investigated modifications a design proposal for the modified exhaust duct system is defined in order to enable stable test operation of the engine-propeller propulsion system.

Different test facility geometries were analyzed with CFD simulations for explaining the observed effects and to give recommendations for test cell modification. Even though test cell optimization with CFD methods started more than 20 years ago for indoor-propeller test cells [3] there is little information to be found in literature related to this topic.

NUMERICAL METHODS AND MESHING

The CFD simulations were carried out with the CFX solver in the current workbench environment of ANSYS and the mesh was created with the workbench tool. It was necessary to simplify the numerical calculations around the propeller to achieve a high mesh resolution and therefore a high accuracy at the inlet of the duct system. The complete geometry of the aero engine test facility shown in Figure 1 A, B was used to build a tetrahedral mesh. Figure 1 C shows the created computational domain. The mesh refinements were adapted to the known flow topology. Minimizing element distortion and a required resolution in high gradient regions were considered.

Turbulence was modeled with the Shear-Stress-Transport-Modell (SST), which was provided by ANSYS-CFX. The complete flow field in the test-stand was considered as a turbulent flow. Laminar turbulent boundary layer transitions were not taken into account. CFD simulations with the used SST model are able to predict flow separation on walls as well as on sharp edges [4], [5].

Previous to the numerical simulation like the present one, it was calculated roughly, how long it takes a fluid particle to pass the complete test facility. With this value (12 s), the time steps of the numerical calculation were estimated. At least after this time stable results in the facility under constant boundary conditions can be expected. The distance a particle has to travel is approx. 60 m (including length and height of the facility) and the averaged flow velocity in the area of the major cross-section is approx. 5 m/s. The presented results were calculated with a physical timescale of 0.1 seconds and 2000 iteration steps, which correspond to app. 3.5 minutes in real-time. The simulation was conducted with the “Physical Timesteps” model of ANSYS-CFX which is a nearly unsteady approach. Iteration steps can be interpreted as time steps but an analysis in the time domain or a frequency analysis of the results are not valid. Hence, it is a steady state calculation with unsteady characteristics, but it is not an URANS simulation.

The selected convergence criterion was 10^{-4} and the convergence target was set to 1 % for variations of mass- and momentum-flows. The Mesh quality was evaluated by mesh orthogonally, expansion factor and aspect ratio. The minimum orthogonal angle was between 50° > 20°, the maximum mesh expansion factor was < 20.0, the maximum aspect ratio was < 100. The number of nodes on the disc was set to 5000 in order to ensure the accurate reading of the velocity components. The calculation with approx. 5 million elements on an 8 core workstation took 12 hours. At the end of the simulation the maximum inaccuracy of the mass balance was less than 10^{-4} and the momentum balance less than 10^{-3}. The imbalances varied by ± 0.1%.

For the flow field of the propeller, a calculation model with a main velocity and a swirl distribution was adopted in the RANS model (sink/source approach). The simulation of the flow field in the test-bed was carried out with a thin disk (momentum and swirl source) instead of the real propeller with known inlet and outlet conditions of the 2-dimensional flow velocity in axial and circumferential direction. With an assumed distribution of the propeller pressure rise the velocity in circumferential direction was calculated in accordance to the Euler turbo-machine equation with no inlet swirl:

$$c_{2u} = \frac{\Delta p}{\rho \ u_2} \qquad (1).$$

A radial distribution of the pressure rise was not given. Thus, an assumed distribution with a maximum at 75% rotor blade length and a 15% hub area was generated and is shown in Figure 3. The pressure distribution function

$$\Delta p = \frac{p_0}{1-r}\left(1-e^{-\frac{1-r^2}{t_p}}\right) \qquad (2)$$

and the distribution function of the axial flow velocity

$$c_z = \frac{c_{z0}}{1-r}\left(1-e^{-\frac{1-r^2}{t_{cz}}}\right) \qquad (3)$$

are similarly designed as the velocity profile of a Hamel-Oseen-Vortex. In such a way pressure and velocity distributions could be added to the CFD calculation as boundary conditions of a typical propeller. The constants p_0, c_{z0}, t_p and t_{cz0} were calculated in an iterative way with a known averaged pressure rise with respect to an area averaging of the pressure distribution. Figure 4 and 6 show the distributions in use of the velocity components.

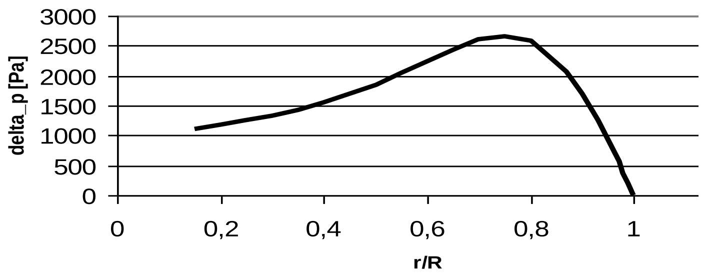

Figure 3: Assumed pressure distribution along the blade length.

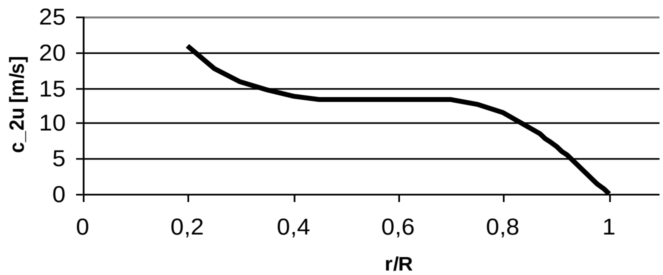

Figure 4: Circumferential flow speed component c_2u at rotor outlet.

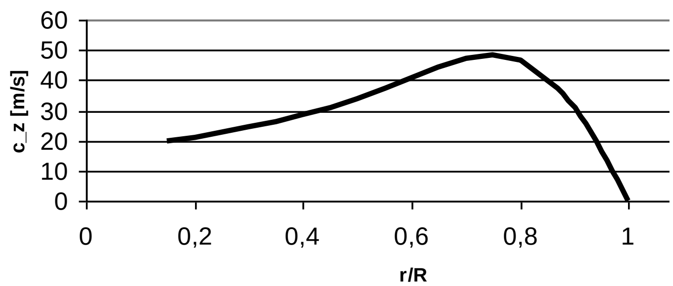

Figure 5: Axial flow speed component at rotor outlet.

In Figure 6 the velocity components x, y, z and a vector preview of the implemented source are depicted. The component z equals the axial flow speed component at the rotor outlet with a maximum of 50 m/s at 75% of the radius.

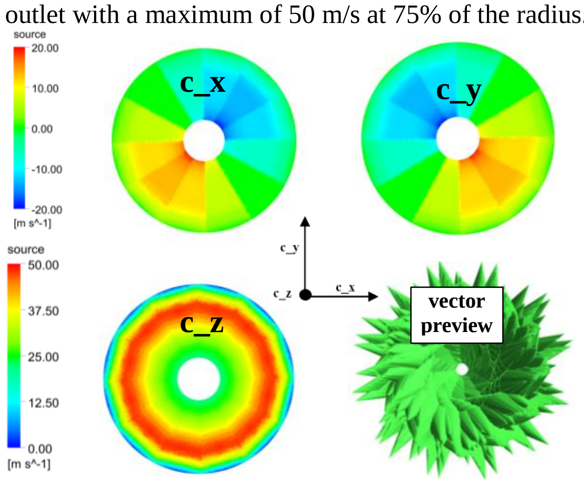

Figure 6: Velocity components x, y, z and the vector preview, disc diameter = 2.1 m, <u>disc outlet view</u>.

FLOW FIELD IN THE TEST CELL WITH PROPELLER OPERATION

The test facility was operated with many different engine-propeller propulsion systems in the past. Due to the asymmetric design of the test stands inside the test cell the rotational direction of the propeller (clockwise or anti-clockwise) has an influence on the flow inside the test cell. Most of the propeller engine configurations operated in the past were propulsion systems rotating clockwise.

Figure 7 shows the flow field in the original configuration of the test facility with the boundary conditions for a propeller with 2.1 m in diameter operating anti-clockwise. The air mass flow of 134 kg/s passing the propeller is the desired mass flow passing the test facility from inlet to the exhaust chimney in order to avoid significant secondary flows inside the test cell. Therefore, a comparison of the propeller air mass flow (q_{m_target}) with the air mass flow passing the exhaust chimney ($q_{m\_exhaust}$) is chosen as an evaluation and optimization criterion for test cell modifications and configurations. All data is summarized for the investigated configurations in Table 2. In comparison to the measured flow topology in Figure 2 the numerical results fit quite well. There is an intensively influenced flow field inside the test cell since only a small portion of the mass flow from the propeller mock-up is passing through the related propeller test stand exhaust duct “a)” (approx. 21 %). In addition to the effect of the propeller exhaust duct dimensions are not capable to catch the mass flow from the propeller, the rotating direction of the propeller and the wall of the test cell push the flow “upwards” regarding the view top in Figure 7**.**

The open connection way which is combining the flow of the two chimneys “a)” and “b)” adds additional losses. A part of the mass flow passing the chimney is sucked through the second exhaust chimney system “b)” used for the turbojet test stand. Generally, the propeller operates with a significantly choked outlet duct flow resulting in a large recirculation zone in the test cell (dashed line RZ 1). Both recirculation zones RZ 1 and RZ 2 are unstable by means of the rectangular room geometry. Thus, another small flow separation zone RZ 3 in the exhaust duct “a)” is created.

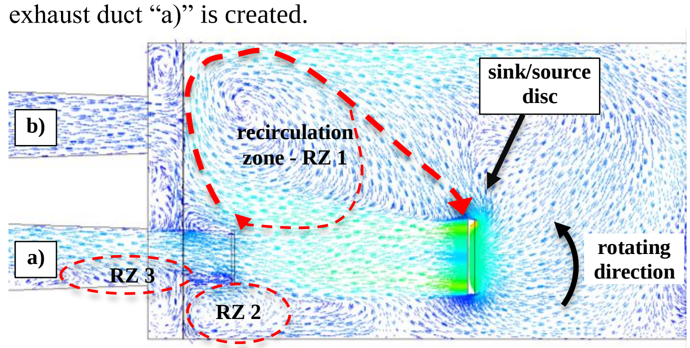

Figure 7: Original configuration, rotor diameter 2.1 m, q_{m_target} = 134 kg/s, $q_{m\_exhaust}$ = 28.1 kg/s, anti-clockwise rotation, <u>view from top</u>.

A closer look at the mass flow in the exhaust duct “a)” gives Figure 8. The mass flow is plotted over the time step number of

a transient CFD simulation (0.1 s for each timestep). Instead of the strong fluctuations of the rotational speed in the real test rig (see Figure 20), heavy mass flow fluctuations in the exhaust duct become visible. Thus, the following explanation for the unsteadiness of the system can be made:
At the beginning the flow of the disc (in CFD) or the propeller (in reality) hits the exhaust duct straight on which leads to high mass flows in the duct. By means of the fact that not the entire mass flow can pass the duct, large recirculation zones form inside the test cell. Through the rectangular room geometry these zones become unstable and lead to an upwards deflection of the main flow as shown in Figure 7. This deflection in turn leads to a smaller mass flow in the exhaust duct. Afterwards the RZ 1 and RZ 2 create a deflection in the opposite direction. This causal chain causes a periodic up- and downward motion of the main flow and thus an unstable flow regime inside the test cell.

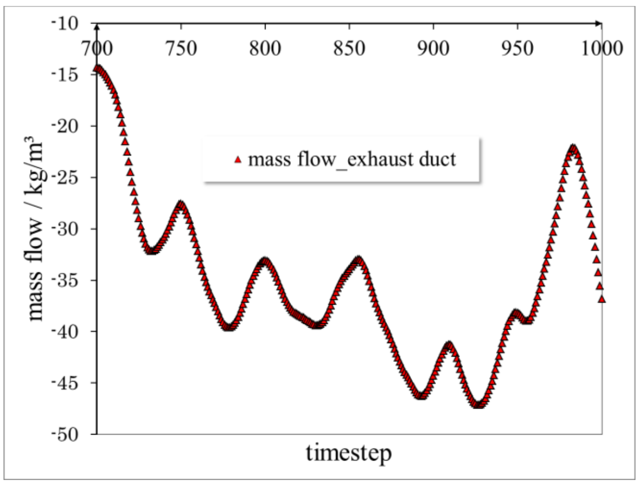

Figure 8: Original configuration, rotor diameter 2.1 m, q_{m_target} = 134 kg/s, $q_{m\_exhaust}$= 15-45 kg/s, anti-clockwise rotation, mass flow and static pressure over timestep 700-1000 (timestep length = 0.1 s).

OPTIMIZATION OF THE DUCT SYSTEM AND THE COLLECTOR

As a first step for optimization it is necessary to reduce the influence of the second exhaust chimney and the connection way. Hence, both parts were neglected in the simulation (see Figure 9). As before, three recirculation zones form inside the test cell due to the swirl in the air flow and the exhaust duct entrance "a)" which is not capable to catch the flow completely. Compared to the configuration with the open exhaust chimney connection way this facility modification results in an increased exhaust mass flow of $q_{m\_exhaust}$= 34.4 kg/s which corresponds to 26 % of q_{m_target}. Nevertheless more significant modifications of the exhaust duct geometry are required to optimize the flow field in the test cell introducing a collector behind the propeller.

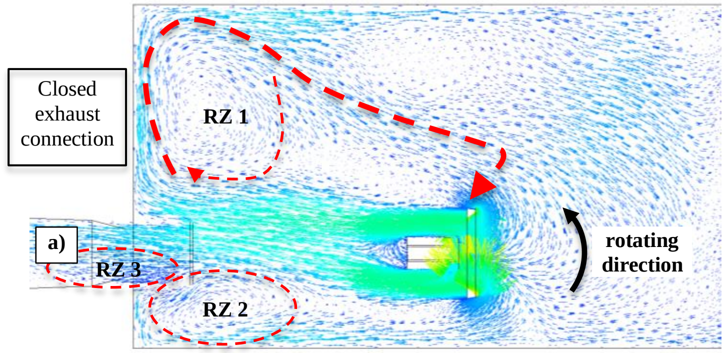

Figure 9: Configuration with closed exhaust connection way (impact loss reduction), rotor diameter 2.1 m, q_{m_target} = 134 kg/s, $q_{m\_exhaust}$ = 34.4 kg/s, anti-clockwise rotation, view from top.

The flow topology of the first two configurations indicated that a collector cone has to be designed for the inlet of the exhaust duct system. Three different collectors have been investigated. All collectors are designed as rectangular geometries due to the squared geometry of the existing 1.6 x 1.6 m area of the exhaust chimney duct system. Again the comparison of the air mass flow passing the propeller (q_{m_target}) and the air mass flow passing the exhaust chimney ($q_{m\_exhaust}$) are chosen as an optimization criterion for test cell modifications.

Collector A was designed with an open area increased by a factor of 2.4 compared to the original configuration. The collector overlaps app. 0.5 m into the test cell, shown in Figure 10 to avoid interference effects with the walls of the test cell. The collector inlet has a cross-section of 2.2 x 2.2 m and the outlet connects to the existing 1.6 x 1.6 m area of the duct system. Using this collector the exhaust flow rate was increased by up to 65% of the target mass flow rate ($q_{m\_exhaust}$= 87 kg/s). The side view inside the test cell shows that the propeller flow field is directed towards the ceiling of the test cell through interference effects with the walls of the test cell. Therefore significant asymmetric recirculating flows establish next to the ground and the ceiling influencing the flow field.

There is still a significant amount of air recirculation inside the test cell. Therefore, the open area of the collector needs to be further increased.

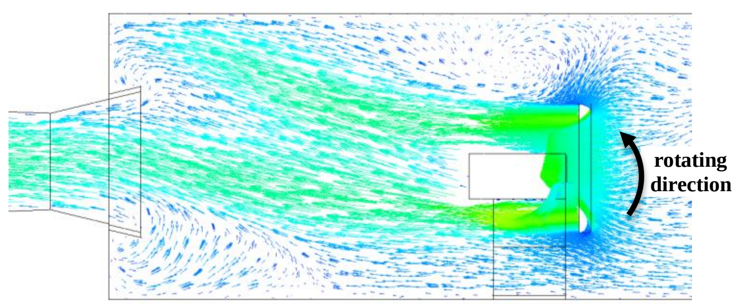

Figure 10: Configuration with collector A (0.5 m overlap in the test cell and closed exhaust connection way), rotor diameter 2.1 m, q_{m_target} = 135 kg/s, $q_{m\_exhaust}$ = 87 kg/s, anti-clockwise rotation, side view.

A first redesign of the collector is shown in Figure 11 (collector B). The length of the collector was significantly enlarged overlapping app. 2.7 m into the test cell. The inlet cross-section was scaled up to 3 x 3 m resulting in an open area increased by a factor of 4.5 compared to the original configuration.

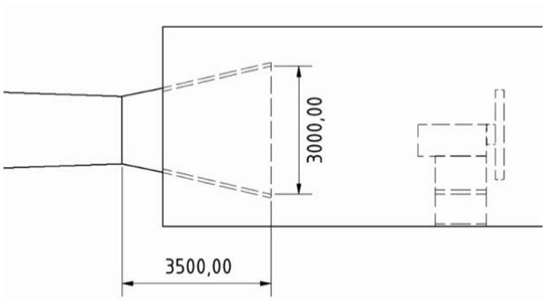

Figure 11: Design of the collector B - extended in the test-stand with increased inlet (3 x 3 m), outlet 1.6 x 1.6 m, side view.

Figure 12 shows the flow field in the collector B configuration in the mid-plane section with view from top. Most of the air mass flow of the propeller passes through the exhaust duct. The exhaust flow rate of 133.5 kg/s nearly meets the target mass flow passing the propeller (99 %).

The flow field inside the test cell is more homogenous, especially the large recirculation zone RZ 1 is significantly reduced. Inside the collector B a local recirculation zone can be identified, but the open area of the collector is large enough to compensate for the area which is aerodynamically blocked. Also the side view of the flow inside the test cell (Figure 13) shows that most of the propeller mass flow is captured by collector B. The mass flow close to the ground which is not passing the collector indicates that a further increased inlet area of a collector is necessary.

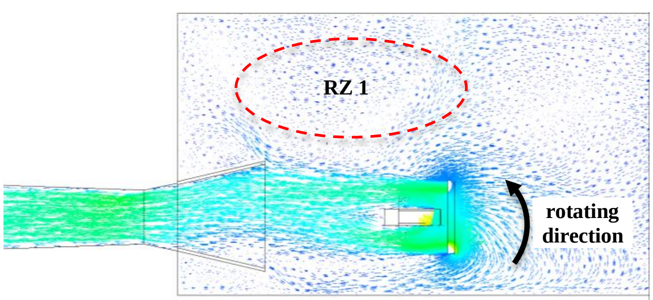

Figure 12: Configuration with collector B (extended in the test-stand, closed exhaust connection way), rotor diameter 2.1 m, q_{m_target} = 134 kg/s, $q_{m\_exhaust}$ = 133.5 kg/s, anti-clockwise rotation, view from top.

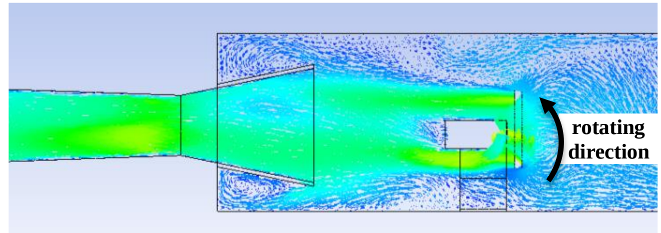

Figure 13: Configuration with collector B (extended in the test-stand, closed exhaust connection way), rotor diameter 2.1 m, q_{m_target} = 134 kg/s, $q_{m\_exhaust}$ = 133.5 kg/s, anti-clockwise rotation, side view.

Since the test facility modification must be capable of operating with different rotational directions, a simulation with an opposite rotational direction of the propeller is required, Figure 14. In this configuration the exhaust flow rate of 114 kg/s is only 85% of the target mass flow. The opposite swirl direction of the propeller flow shows an interference with the side wall of the test cell resulting in an enlarged recirculation zone RZ 2 inside collector B directed towards the open test cell area. These flow phenomena create an intensified recirculation zone inside the test cell compared to the anti-clockwise configuration. Increasing the open area at the inlet and reducing the length the collector can reduce this effect.

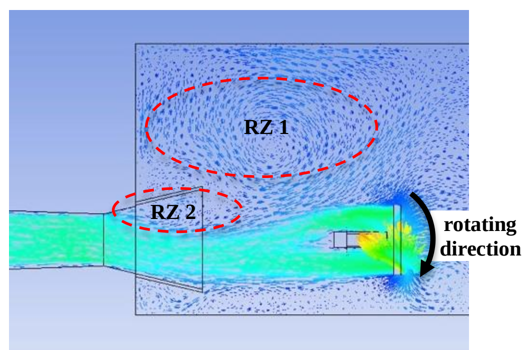

Figure 14: Configuration with collector B (extended in the test-stand, closed exhaust connection way), rotor diameter 2.1 m, q_{m_target} = 134 kg/s, $q_{m\_exhaust}$ = 114 kg/s, clockwise rotation, view from top.

The test stand modification must also be capable of operating with a wide range of propeller sizes. Therefore a smaller propeller configuration of 1.6 m diameter at a mass flow rate of 52 kg/s passing the propeller was investigated assuming the same boundary conditions as shown in Figure 3, Figure 4 and Figure 5.

Figure 15 shows the 3-D flow field as well as the selected streamlines for the 1.6 m propeller mock-up with collector B. In the area of the second engine test bed there is still a slight recirculation zone RZ 1 visible but the exhaust flow rate of 52 kg/s meets the target mass flow passing the propeller (100%).

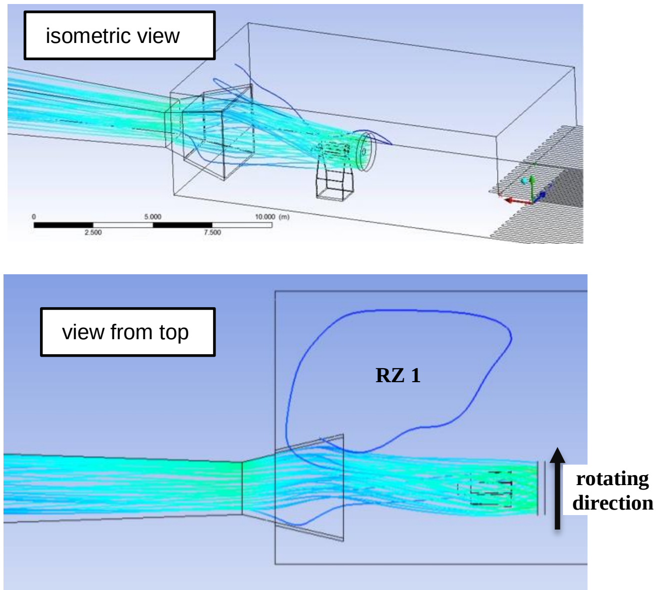

Figure 15: Selected streamlines of collector B configuration (extended in the test-stand, closed exhaust connection way), rotor diameter 1.6 m, q_{m_target} = 52 kg/s, $q_{m\_exhaust}$ = 52 kg/s, anti-clockwise rotation, <u>isometric view</u> and <u>view from top</u>.

Additional boundary conditions of the test cell for installing the collector cone in the test facility are considered. This requires a shorter collector cone at maximum of 3 meter length. The collector cone is also used as an emergency exit but installations of the cooling water and the electrical systems limit the design space. Hence a shorter version of collector B is required.

Bringing together all design requirements a new collector configuration C was defined. Figure 16 shows the enlarged inlet cross-section of 3.5 x 3.5 m and shortened length of the collector.

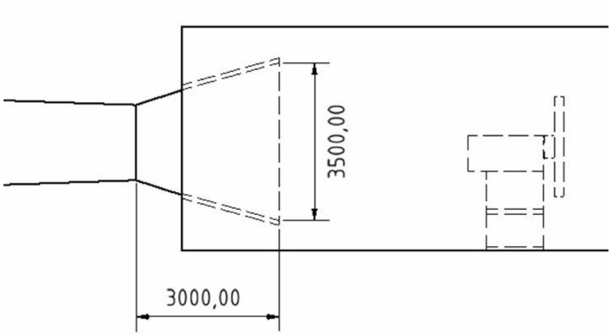

Figure 16: Design of the shortened collector C with further increased inlet (3.5 x 3.5 m), outlet 1.6 x 1.6 m, <u>side view</u>.

The mid-plane view from top in Figure 17 shows a comparable flow topology as collector B. Inside the test cell a quite homogenous flow topology can be found where no significant recirculation zone establishes. Inside collector C a local recirculation zone can be identified, but the open area of the collector is still large enough to compensate the flow blockage by the recirculating flow.

In Figure 18 the side view of the flow field shows that not the complete mass flow passing the propeller is entering the collector due to the reduced collector length. Recirculation zones created by the interference of the ground and the ceiling of the test cell are equally distributed resulting in a more homogenous flow field compared to collector A, Figure 10.

In configuration C the exhaust flow rate of 128 kg/s is reduced to 95% of the target mass flow, which is still acceptable considering the flow topology inside the test cell.

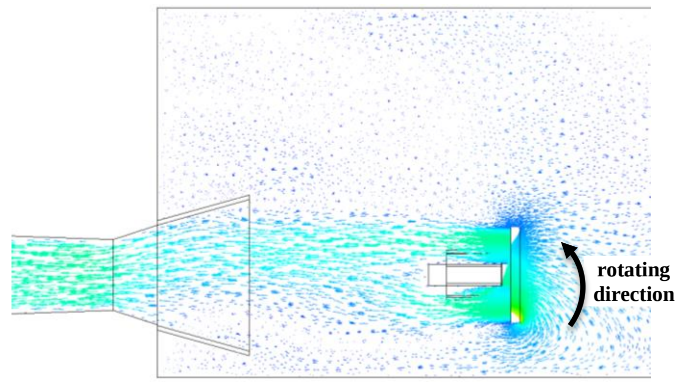

Figure 17: Configuration with collector C (increased inlet), rotor diameter 2.1 m, q_{m_target} = 134 kg/s, $q_{m\_exhaust}$ = 128 kg/s, anti-clockwise rotation, <u>view from top</u>.

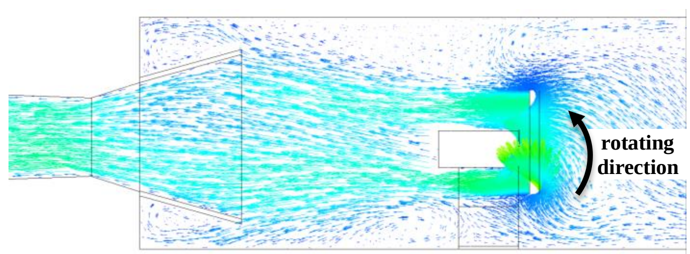

Figure 18: Configuration with collector C (increased inlet), rotor diameter 2.1 m, q_{m_target} = 134 kg/s, $q_{m\_exhaust}$ = 128 kg/s, anti-clockwise rotation, <u>side view</u>.

Table 2 summarizes the investigated configurations and the comparisons of the exhaust flow rate and the related target mass flow. It is expected that an unsteady simulation (URANS) would be much more accurate in simulating the exact mass flow values and flow phenomena. Due to the flow separation the recirculation areas within the facility itself and in the collector cone the real flow has an unsteady characteristic.

Table 2: Summary of the shown configurations.

Configuration	q_{m_target} kg/s	$q_{m\_exhaust}$ kg/s
Original Configuration anti-clockwise, D = 2.1 m	134.0	28.1
Closed exhaust connection anti-clockwise, D = 2.1 m	134.0	34.4
Collector A anti-clockwise, D = 2.1 m	135.0	87.0
Collector B anti-clockwise, D = 1.6 m	52.0	52.0
Collector B clockwise, D = 2.1 m	134.0	114.0
Collector B anti-clockwise D = 2.1 m	134.0	133.5
Collector C anti-clockwise D = 2.1 m	134.0	128.0

Collector C was chosen to be implemented in the test facility based on the numerical findings and design limitations considering test cell integration. Despite the given limitations the numerical results were very helpful to find an adequate design for the test facility design modification. Figure 19 shows the modified test cell with the designed collector C, the closed exhaust duct system and the installed propulsion system RED A03.

Figure 19: Modified test cell with collector C and closed exhaust duct system with propulsion system RED A03 installed.

After implementing collector C the periodic fluctuations of the propeller flow were eliminated and the test cell now allows for a stable operation of the new propulsion system up to full load Take-Off power which was not possible with the original configuration of the test cell.

Figure 20 shows a comparison of the rotational propeller speed before (-- w before Mod) and after (- w after Mod) the modification of the test cell at part load operation of the propulsion system. The propeller rotational speed is stable with the test cell modification. Also the stable time averaged point of operation at given engine power can be shown by the increased fuel flow (Figure 20, ····· FF after Mod) compared to the point of operation in the original test cell configuration (Figure 20, -· FF before Mod). The unstable behavior of the rotational speed is similar to the calculated mass flow fluctuations which can be observed in Figure 8.

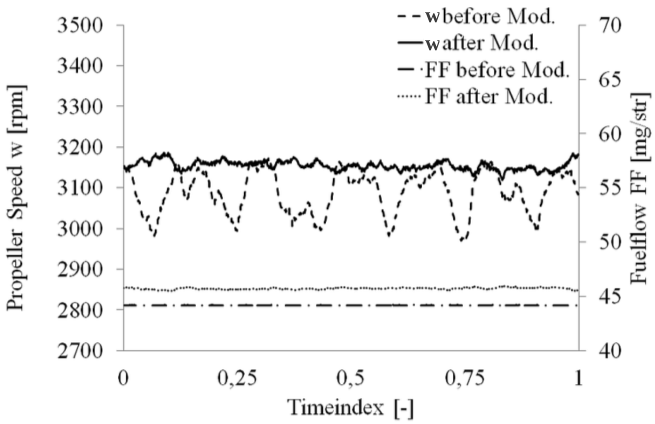

Figure 20: Periodic fluctuations of the rotational speed of the propeller and piston engine fuel flow before and after the modification of the test cell.

CONCLUSION

An aviation propulsion system configuration with a propeller configuration at high flow rates is investigated in an indoor engine test facility. Vibrations of the propeller and fluctuations in the propeller rotational speed were observed during operation of the propulsion system making a steady state operation of the propeller unfeasible.

Numerical flow simulations and measurements of the characteristic flow field inside the test facility showed a large unstable recirculation zone. This zone was covering a significant area of the test cell. Through a backwards recirculation of the flow into the inlet of the propeller, the rotational speed fluctuations were caused. Some area of the outlet duct of the test facility was aerodynamically blocked enhancing the test cell recirculation.

For a ranking of several possible improvements a simplified CFD simulation was carried out with a new approach for the propeller flow field. The sink/source approach permits a high accuracy of the flow topology and the pressure loss calculations through a comparatively high mesh resolution in the duct system and the test cell - no propeller mesh is necessary

Furthermore, this approach with its radial distribution of the outlet swirl is not known from the literature and has not been published before. In particular, the radial distribution of the swirl was designed according to the velocity profile of a Hamel-Oseen-Vortex with a typical maximum at 75% rotor span.

An important parameter for the rating of the optimization was the mass flow balance from the inlet to the outlet of the complete duct system with several openings. Three collector configurations are studied to optimize the flow field inside the test cell.

Since the test facility modification must be capable of operating with smaller propeller sizes and varying rotational directions of the propeller one promising collector configuration is studied.

Despite the given limitations of the numerical method the results were very helpful to find an adequate design for the test facility modification. The final configuration of the collector is based on the findings of the simulations and the design constraints defined by the integration into the test cell.

After implementing the new optimized collector in the test facility the periodic fluctuations of the propeller flow were eliminated and the test cell allows a stable operation of the propulsion system up to full load Take-Off power.

NOMENCLATURE

Latin letters

BSFC	[g/KWh]	Brake Specific Fuel Consumption
c_{2u}	[m/s]	Absolute Air Velocity At The Propeller Outlet In Circumferential Direction
$c_{\_az}$	[m/s]	Axial Flow Velocity
$c_{x,y,z}$	[m/s]	Absolute Air Velocity in x, y, z-Direction
c_{z0}	[m/s]	Absolute Air Velocity in z-Direction at Inlet
D	[m]	Propeller Diameter
FF	[mg/str]	Fuel Flow
Δp (delta_p)	[Pa]	Differential Pressure
p_0	[Pa]	Ambient Pressure
q_{m_target}	[kg/s]	Target Air Mass Flow passing the propeller
$q_{m\_exhaust}$	[kg/s]	Air Mass Flow passing the exhaust chimney
r	[m]	Relative Radial Position on Propeller Blade
R	[m]	Total Propeller Radius
u_2	[m/s]	Relative Velocities at the Outlet
w	[rpm]	Propeller Rotational Speed

Greek letters

ρ_{u2}	[kg/m³]	Fluid Density

Abbreviations

EECU	Electronic Engine Control Unit
FL	Flight Level
DOHC	Double Over-Heat Camshaft
SL	Sea Level

REFERENCES

[1] “Design Considerations for Enclosed Turboprop Engine Test Cells”, SAE Standard AIR5295, issued 1998-10, revised AIR5295A issued 2013-10.

[2] Ostenrath, H., Gerber, G., “Schallschutzmaßnahmen an einem Flugtriebwerksprüfstand“, Zeitschrift für Lärmbekämpfung 27, 62-67 (1980), Springer Verlag, Berlin 1980.

[3] Daley, P. L., Mahaffey, W. A., “Structured Finite Volume Modeling of U.S. Navy Aircraft Engine Test Cells, Task 2: Turboprop Engine – Final Report – Volume 1“, June 1993.

[4] Mentera, F. R., “Review of the Shear-Stress Transport Turbulence Model Experience from an Industrial Perspective”, International Journal of Computational Fluid Dynamics, Volume 23, Issue 4, 305-316.

[5] Kameier, F., Horvat, I., Becker, K., “Konventionelle CFD für strömungsakustische Optimierung“, 2010, DAGA Berlin.